Laboratory characterization of a mode-selective photonic lantern for exoplanet characterization

Yinzi Xin[a], Daniel Echeverri[a], Nemanja Jovanovic[a], Dimitri Mawet[a,b], Sergio Leon-Saval[c], Rodrigo Amezcua-Correa[d], Stephanos Yerolatsitis[d], Michael P. Fitzgerald[e], Pradip Gatkine[a], Yoo Jung Kim[e], Jonathan Lin[e], Barnaby Norris[f], Garreth Ruane[b], and Steph Sallum[g]

[a]Department of Astronomy, California Institute of Technology, 1200 E California Blvd, Pasadena, CA, 91125, USA
[b]Jet Propulsion Laboratory, California Institute of Technology, 4800 Oak Grove Drive, Pasadena, CA, 91109, USA
[c]Sydney Astrophotonic Instrumentation Laboratory, School of Physics, The University of Sydney, Sydney, NSW 2006, Australia
[d]The College of Optics and Photonics, University of Central Florida, 4304 Scorpius St, Orlando, FL 32816
[e]Department of Physics & Astronomy, 430 Portola Plaza, University of California, Los Angeles, CA 90095, USA
[f]Sydney Institute for Astronomy, School of Physics, Physics Road, The University of Sydney, NSW 2006, Australia
[g]Department of Physics & Astronomy, University of California, Irvine, 4129 Frederick Reines Hall, Irvine, CA 92697 USA

ABSTRACT

Coronagraphs allow for faint off-axis exoplanets to be observed, but are limited to angular separations greater than a few beam widths. Accessing closer-in separations would greatly increase the expected number of detectable planets, which scales inversely with the inner working angle. The Photonic Lantern Nuller (PLN) is an instrument concept designed to characterize exoplanets within a single beam-width, using a device called the mode-selective photonic lantern (MSPL), a photonic mode-converter that maps linearly polarized modes into individual single-mode outputs. The PLN leverages the spatial symmetry of an MSPL to create nulled ports, which cancel out on-axis starlight but allow off-axis exoplanet light to couple. However, the quality of the nulls is dependent on the symmetry of the lantern modes, which affects how well the starlight can be suppressed. We present results from our laboratory characterization of an MSPL, including measurements of lantern port throughputs (60-90%), images of the mode intensities, and reconstructions of the mode electric fields using off-axis holography. We discuss the implications on the level of starlight suppression that this MSPL can achieve.

Keywords: photonic lanterns, astrophotonics, nulling interferometry

1. INTRODUCTION

The characterization of exoplanets was identified by the Decadal Survey for Astronomy and Astrophysics 2020 as one of the top scientific priorities.[1] High-resolution spectroscopy is especially critical for many measurements, including that of the planet's radial velocity, spin, atmospheric composition, and surface features through Doppler imaging.[2] It can also enable the potential detection of exomoons.[3] The Photonic Lantern Nuller[4,5] is an instrument concept that enables the high-resolution spectral characterization of exoplanets at and within 1 λ/D, where λ is the wavelength and D the telescope diameter. It is inspired by the Vortex Fiber Nuller (VFN),[6,7]

Further author information: (Send correspondence to Y.X)
Y.X: E-mail: yxin@caltech.edu

Techniques and Instrumentation for Detection of Exoplanets XI, edited by Garreth J. Ruane, Proc. of SPIE Vol. 12680, 126800I · © 2023 SPIE
0277-786X · doi: 10.1117/12.2676421

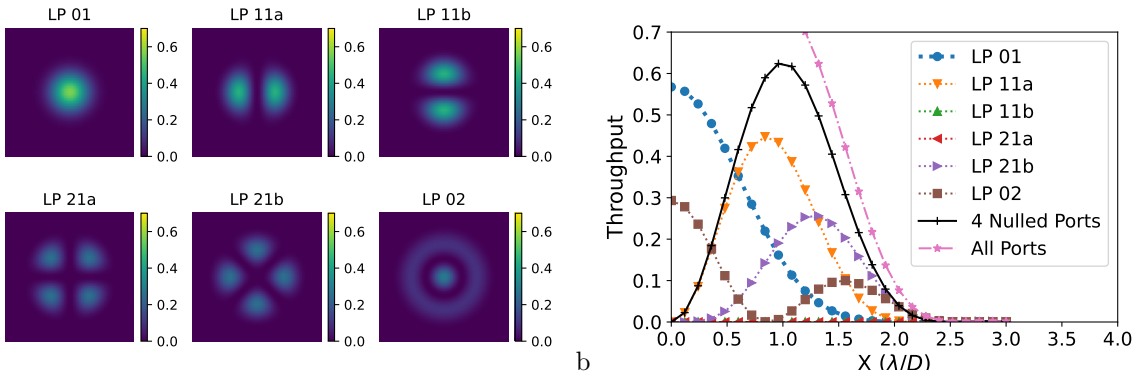

Figure 1. a) Throughput maps for each port of an ideal six-port mode-selective photonic lantern, spanning from -3 λ/D to 3 λ/D in each direction. b) X-axis line profiles from the throughput maps. The four nulled ports are LP 11ab and LP 21ab. The line profile of the summed throughput of the nulled ports is shown in black with cross-hair markers.

but unlike the VFN, which has only one nulled channel with a circularly symmetric coupling profile, the PLN provides four nulled channels, each with a unique coupling profile. This allows for more planet flux to be retained, and also helps place better constraints on the planet's flux ratio and spatial position.[4]

The PLN exploits the symmetries of the ports of a six port mode-selective photonic lantern (MSPL),[8] a special type of photonic lantern[9] that utilizes dissimilar cores that enable ports to be mapped into linearly polarized (LP) modes, or the eigenmodes of a radially symmetric, weakly guiding step-index waveguide. Each mode at the multi-mode face (MMF) of the lantern is mapped to a single-mode fiber (SMF) output, such that light coupling to a given mode at the MMF side will result in flux in the corresponding SMF core. The device is bi-directional, so light injected into one of the SMF ports will propagate into the mode corresponding to that port at the MMF.

The operating principles of the PLN are fully derived in Ref. 4. Here, we summarize the case where a telescope beam is injected directly into MMF of the photonic lantern, without the inclusion of any upstream optics. If we label the LP mode azimuthal order by an integer m analogously to how Zernike polynomials are labeled — i.e. positive m indicating an azimuthal component of $\cos(m\theta)$ and negative m indicating $\sin(m\theta)$ — then, the polar component of the integral that describes the coupling of an unaberrated on-axis telescope beam into a photonic lantern port is given by

$$\begin{aligned} &\int_0^{2\pi} \cos(m\theta)d\theta, \quad m \geq 0, \quad \text{or} \\ &\int_0^{2\pi} \sin(m\theta)d\theta, \quad m < 0. \end{aligned} \tag{1}$$

This polar integral will integrate to 0 and result in an on-axis null *except* when $\pm m = 0$. For a six port MSPL, the LP 01 and LP 02 ports (which have $m = 0$) are non-nulled, while the LP 11a ($m = 1$), LP 11b ($m = -1$), LP 21a ($m = 2$), and LP 21b ($m = -2$) ports are nulled. The simulated spatial throughput maps for each port of an ideal six port MSPL are shown in Figure 1a. As seen in the x-axis cross-section shown in Figure 1b, the summed throughput from all four nulled ports given an off-axis planet at 1.0 λ/D is $\sim 60\%$.

However, a real photonic lantern will not have the ideal mode shapes that correspond to perfect LP modes, and the device itself will have some additional throughput loss. In this work, we characterize the properties of a real photonic lantern, including manufacturing imperfections. We then integrate it into a testbed to demonstrate the PLN in the lab.

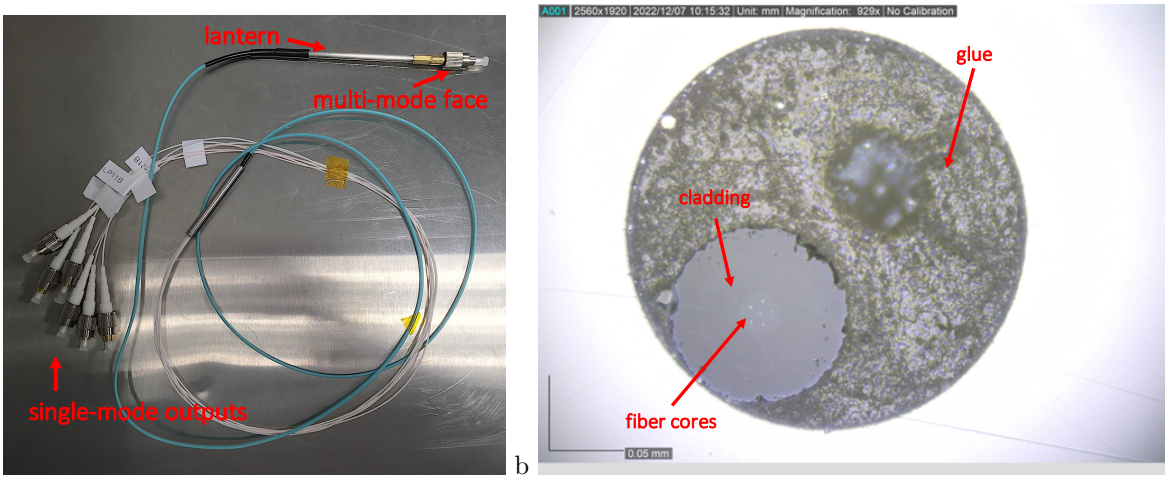

a b

Figure 2. a) A picture of a six-port MSPL. The lantern is the stiff silver portion in the top right, with the MMF facing towards the right. Each SMF output of the lantern is connected to one of the white fiber pigtails. b) A microscope image of the MMF taken with a Dino-Lite Edge 3.0. The fiber cores are arranged in a pentagonal pattern, visible towards the bottom left as small white circles. The cores are embedded in the cladding, visible as the smooth gray circle. Surrounding the cladding is the glue attaching it to the connector.

2. LANTERN CHARACTERIZATION

A picture of a six-port MSPL is shown in Fig. 2a. The lantern is the stiff silver portion in the top right, with the MMF facing towards the right. Each SMF output of the lantern is connected to one of the white fiber pigtails. We first characterize the properties of this lantern on its own by taking microscope images of the MMF interface, measuring the throughput through each port, and using an interferometer to reconstruct the mode shapes corresponding to each port.

2.1 Microscope Imaging of Lantern Interface

We use a Dino-Lite Edge 3.0 microscope to image the multimode interface of the lantern, show in Fig. 2b. The fiber cores are arranged in a pentagonal pattern, visible towards the bottom left as small white circles. The cores are embedded in the cladding, visible as the smooth gray circle. Surrounding the cladding is the glue attaching it to the connector. The microscope image verifies the expected arrangement of the cores for the mode-selective lantern design presented in Ref. 8.

2.2 SMF to MMF Throughput Measurements

Next, we measured the throughput of each of the lantern's ports from the single-mode inputs to the MMF using a Thorlabs S122C power meter and a Thorlabs KLS1550 laser diode as the light source. We first took a background measurement with the light turned off. Next, we took a measurement of the power coming out of the fiber directly connected to the laser. Then, we connected the light source fiber to one of the SMF pigtails of the photonic lantern and measured the power coming out of the MMF. After background subtracting the measurements, we take the ratio of the power coming out of the MMF to the power coming out of the source fiber to be the throughput of that port. We repeat this process five times for each port, and report the mean and standard deviation of those five measurements in Table 1. Note that these throughput measurements are of the entire lantern assembly, including any connectorization losses or losses through the SMF pigtails, such as Fresnel loss and propagation loss.

2.3 Characterization of Modes

We use a technique called off-axis holography (OAH)[10] to measure the complex electric field corresponding to each of the lantern's ports. A picture of our optical setup for OAH is shown in Fig. 3. The light from a Thorlabs TLX2 tunable narrow linewidth laser (set to a wavelength of 1568.772 nm) is split by a polarization-maintaining

Table 1. The average and standard deviation of five throughput measurements for each lantern port. Note that these throughput measurements are of the entire lantern assembly, including any connectorization losses or losses through the SMF pigtails, such as Fresnel loss and propagation loss.

Port	Throughput	Standard Deviation
LP 01	0.886	0.013
LP 11a	0.890	0.013
LP 11b	0.778	0.017
LP 21a	0.583	0.009
LP 21b	0.614	0.022
LP 02	0.617	0.014

(PM) splitter, which sends half the light to the imaging arm of the interferometer, and the other half to the reference beam arm. The light in the imaging arm goes through a polarization controller, then to one of the single-mode inputs of the MSPL. The light coming out of the MMF of the lantern goes through a lens that collimates the beam, then to a lens that focuses the image onto a First Light C-RED 2 camera.

The light in the reference beam path passes through a PM fiber coil (to increase the path length so it is closer to that of the lantern arm), then through a lens that forms a Gaussian beam large enough to cover the entire lantern mode image. This reference beam interferes with the lantern mode image, creating fringes that allow us to retrieve the complex mode field using Fourier analysis.

To match the polarization between the two arms, the calibration polarizer (shown out of the beam) is first inserted into the reference arm. The polarizer is then fixed to the angle that minimizes the flux of the reference beam on the detector. Then, the polarizer is moved into the lantern arm, and the polarization controller set to minimize the flux that goes through the polarizer and onto the detector. This process aligns the polarization states of both arms to each other.

See Ref. 10 for the principles of using Fourier analysis to retrieve complex amplitudes from off-axis holography. For our work, an example hologram of the LP 21b port (after dark subtraction and centering) is shown in Fig. 4a, and the same hologram zoomed in to the center (such that the fringes are visible) is shown in Fig. 4b. Note that the fringes of interest resulting from interference between the two beams are the fine horizontal ones. The faint, wide, vertical stripes are not from the interference of the two beams, but rather the structure of the reference beam itself, as shown in Fig. 4c. We apply a 2D Fourier transform to the (full-sized) hologram to obtain the Fourier space signal (FFTgram) shown in Fig. 4d. We then isolate the top right lobe of the FFTgram, shown in Fig. 4e.

The cropped lobe in Fig. 4e is centered to minimize the amount of tip-tilt signal in the final reconstructed mode, shown in Fig. 4f. To obtain this final reconstructed mode, we first apply a broad Gaussian window (with a σ of 27 pixels) to the cropped FFTgram to filter out edge effects, then apply an inverse Fourier transform. We then divide by the square-root of the reference beam intensity to remove its impact. Finally, we normalize the mode such that its summed intensity is 1. Because the path length difference between the reference arm and the lantern arm fluctuates widely (due to vibrations and other bench instabilities), we are unable to constrain the global phase of the modes. Fortunately, we do not need to know the global phase to predict the coupled intensities, since they are not impacted by the global phases of each mode.

We apply this same reconstruction process to the other 5 modes of the lantern. We also obtain and analyze three separate datasets taken across multiple days and confirm that the measurements are qualitatively stable. After matching the global phases between the three different measurements, we take their mean and re-normalize each mode to a total intensity of 1 to obtain the final reconstructions, shown in Figure 5. In Section 3.2, the simulated throughput maps from these measured modes are compared to the actual throughput maps obtained on a testbed.

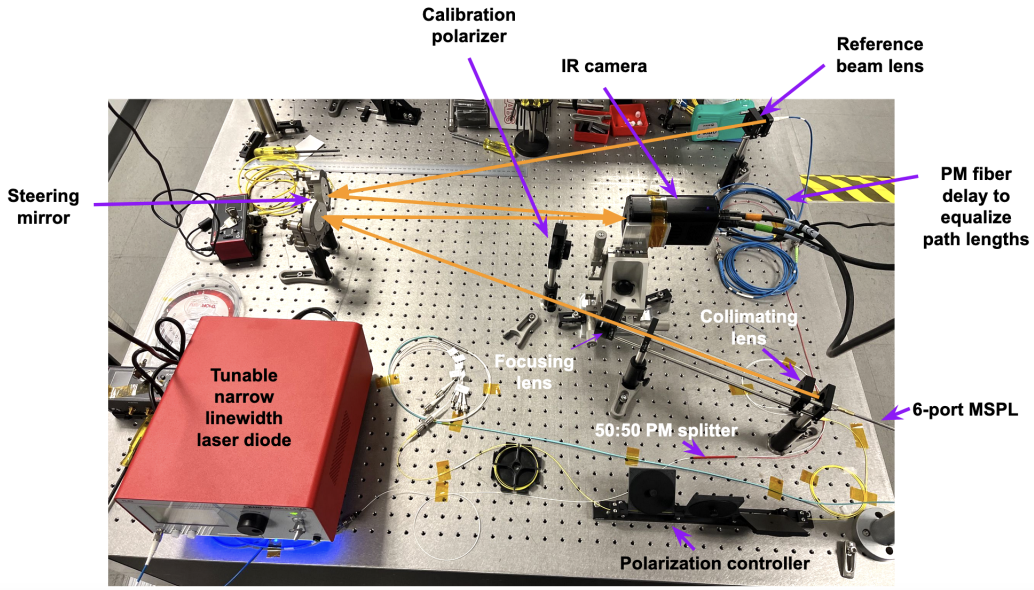

Figure 3. The optical setup for OAH measurements of the lantern modes. The light from a Thorlabs TLX2 tunable narrow linewidth laser (set to a wavelength of 1568.772 nm) is split by a polarization-maintaining (PM) splitter, which sends half the light to the imaging arm of the interferometer, and the other half to the reference beam arm. The light in the imaging arm goes through a polarization controller, then to one of the single-mode inputs of the MSPL. The light coming out of the MMF of the lantern goes through a lens that collimates the beam, then to a lens that focuses the image onto a First Light C-RED 2 camera. The light in the reference beam path passes through a PM fiber coil (to increase the path length so it is closer to that of the lantern arm), then through a lens that turns it into a diverging beam large enough to cover the entire lantern mode image. This reference beam interferes with the lantern mode, creating fringes that allow us to retrieve the complex mode field using Fourier analysis. To match the polarization between the two arms, the calibration polarizer (shown out of the beam) is first inserted into the reference arm. The polarizer is then fixed to the angle that minimizes the flux of the reference beam on the detector. Then, the polarizer is moved into the lantern arm, and the polarization controller set to minimize the flux that goes through the polarizer and onto the detector. This process aligns the polarization states of both arms to each other.

3. PHOTONIC LANTERN NULLER DEMONSTRATION

After characterizing the properties of the MSPL, we integrated it into the Polychromatic Reflective Testbed (PoRT) at Caltech to demonstrate using it as a nuller.

3.1 Experimental Setup

A diagram of the PoRT testbed is shown in Fig. 6. A light source is fed into the bench with a single-mode fiber mounted to the source stage. The light is collimated by an off-axis parabola (OAP) mirror. The collimated light is filtered by a baffle before reflecting off of a 12×12 Boston Micromachines deformable mirror (DM). Then, a set of relay OAPs magnifies the beam. In the resulting collimated beam is a mask mount that can be used to insert a pupil plane mask (such as a vortex); however, we leave it empty for this work. The beam then passes through an adjustable-size iris, which we use to control the $F\#$ of the system. The beam is then focused by the last OAP onto the injection stage, which holds both a single-mode fiber and the 6-port MSPL. The injection stage has translation controllers in all three axes, which allows light to be injected into either the SMF or the MSPL, and can also be used to scan the face of either optic across the focused beam. To measure the coupled flux through the SMF, the output end of the SMF is routed to a Femto OE-200-IN2 photodiode. To measure the coupled flux through one of the lantern ports, the SMF pigtail corresponding to that port is routed to the Femto photodiode. This setup can only measure one port at a time, so the measurements for the different ports are made sequentially.

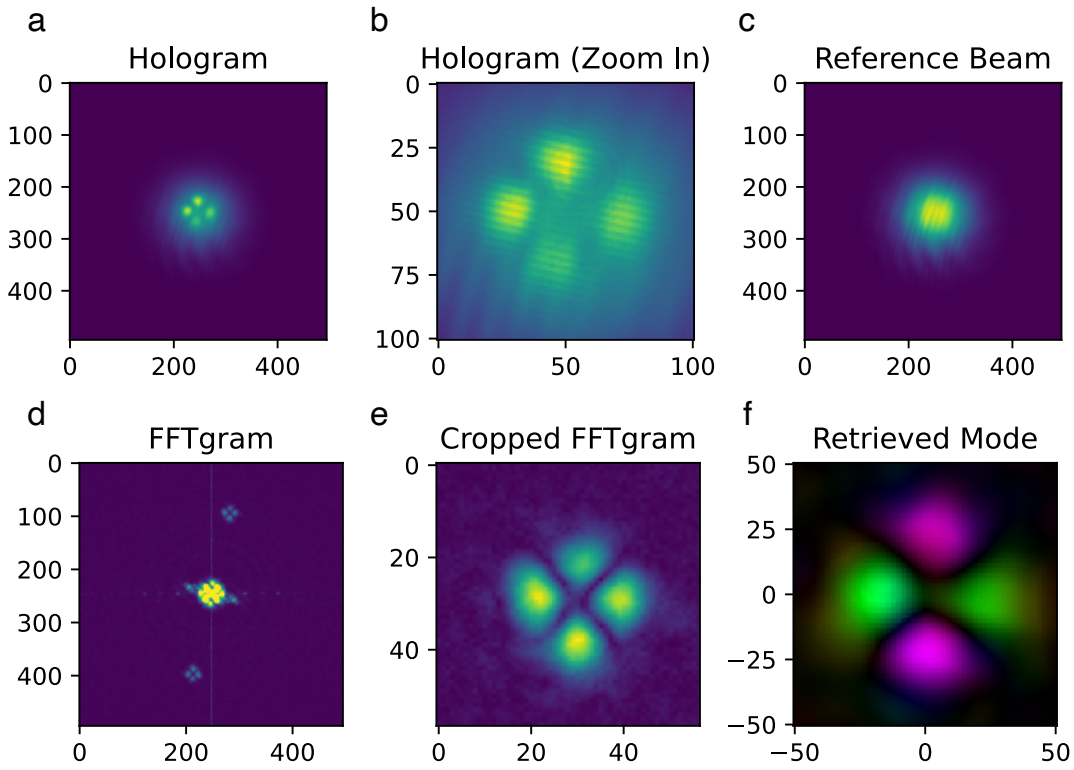

Figure 4. a) The measured hologram of the LP 21b port, centered and background subtracted. b) The same hologram as part (a), but zoomed in to the center to show the fringes. Note that the fringes of interest resulting from interference between the two beams are the fine horizontal ones. c) The reference beam intensity, plotted on the same spatial scale as part (a), showing that the faint, wide, vertical stripes are not from the interference of the two beams, but rather the structure of the reference beam itself. d) The 2D Fourier transform of the hologram in part (a). e) The Fourier-space signal in part (d), cropped to the top right lobe. This lobe is centered to minimize the tip-tilt signal in the final reconstructed mode. f) The final reconstructed mode, obtained by first applying a Gaussian window with a σ of 27 pixels to part (d) to filter out edge effects, then a 2D inverse Fourier transform. The signal is then divided by the square root of the reference beam intensity to remove its impact, then normalized to a total intensity of 1.

A Thorlabs S122C power meter on a retractable stage can be inserted into the beam just before the injection mount to measure its flux, which, after calibrating its readings to that of the Femto photodiode, can be used to normalize the coupled flux measurements to obtain throughput measurements.

We first maximize throughput into the SMF by adjusting the X, Y, and Z directions of the injection stage, the iris size, and by tuning the twelve lowest-order Zernike modes of the DM map. We obtain a peak throughput of 74.1%, whereas the theoretical maximum coupling into a SMF is 82.8%. We have not accounted for Fresnel loss at the face of the fiber and propagation loss through the fiber, which may explain part of the discrepancy. The remaining may be a result of uncalibrated higher order wavefront errors.

Next, we keep the DM map that optimizes injection into the SMF (which implies minimal wavefront aberration), but translate the injection stage to the location of the photonic lantern. We then tune the iris size to maximize the peak off-axis throughput of the LP 11a mode. This is because we expect the contribution to the signal to mostly come from the LP 11 ports, since they have the highest throughput at smaller separations.

In theory, a more complex $F\#$ optimization procedure can be conducted depending on how well the location of the planet of interest is known. The signal-to-noise ratio in a given port depends on both the stellar throughput at the center (η_s) and the off-axis throughput at the planet location (η_p). While η_s also changes as a function of $F\#$, wavefront control can be used to further improve the null without significantly impacting the $F\#$ that

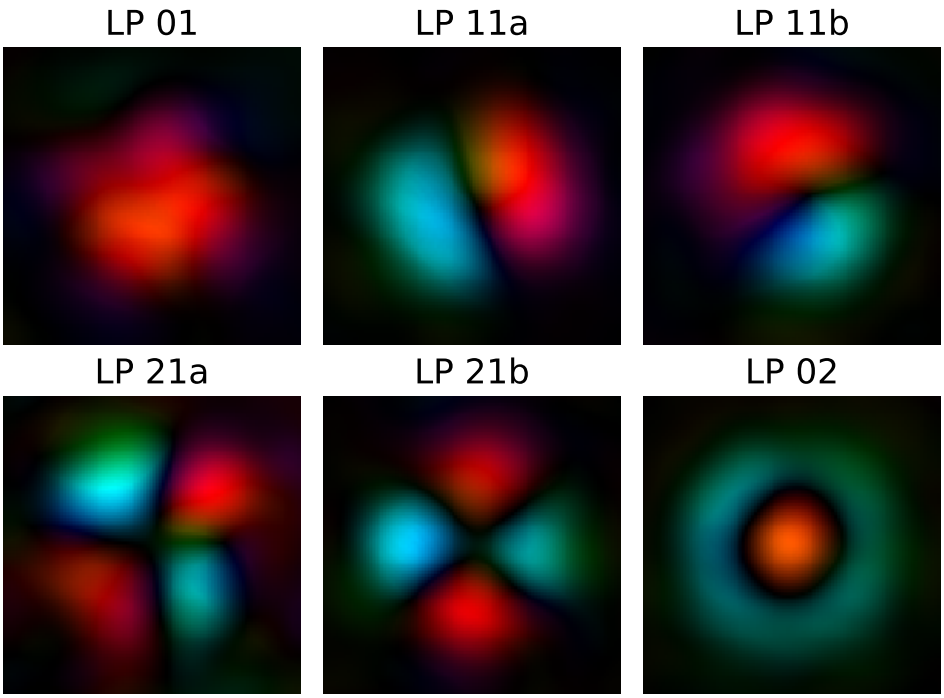

Figure 5. The mean of three measurements of the mode corresponding to each port, obtained using OAH. Because the path length difference between the reference arm and the lantern arm fluctuates widely (due to vibrations and other bench instabilities), we are unable to constrain the global phase of each measurement. Fortunately, we do not need to know the global phase to predict the coupled intensities, since they are not impacted by the global phases of each mode. We thus manually match the global phase of each measurement before taking the mean, then re-normalize such that total intensity of each mode is 1.

would maximize off-axis throughput. Implementing wavefront control with a PLN is left for future work, but because we have additional control over η_s, we choose to optimize iris size for the peak off-axis throughput ($\eta_{p_{\text{peak}}}$) through the LP 11a mode (though the LP 11b mode would be an equally valid choice). In practice, the $F\#$ of an instrument will be fixed to a certain value regardless of the target being observed, and most reasonable optimization metrics targeting close-in planets will result in similar $F\#$'s.

3.2 Results

3.2.1 Monochromatic

We present the PLN throughput maps measured with 1568.772 nm light from the TLX2 tunable narrow linewidth laser on the PoRT testbed in Fig. 7a. The peak off-axis throughput ($\eta_{p_{\text{peak}}}$) of each port is reported in Table 2.

We also simulate throughput maps based on the mode profiles we reconstructed in Section 2.3 (note that the OAH data was taken using the same wavelength as the monochromatic PoRT measurements). We plot the simulated maps in Fig. 7b, on the same color-scale as the PoRT measurements. This simulation assumes that the lantern is flux-preserving — that whatever light gets coupled into a given port is maintained through the lantern. The real lantern assembly is lossy, so has lower throughputs than in simulation. Qualitatively, however, the simulated throughput maps and the measured throughput maps have similar morphologies. Note that in Figure 7b, the simulated throughput maps have been rotated by eye to align with the PoRT measurements. However, the plate scale and XY alignment between the simulations and the measurements have yet to be calibrated to one another, so there is not an exact one-to-one spatial correspondence between the pixels of Figure 7a and those of 7b. The calibration and alignment between the two sets of maps will require determining

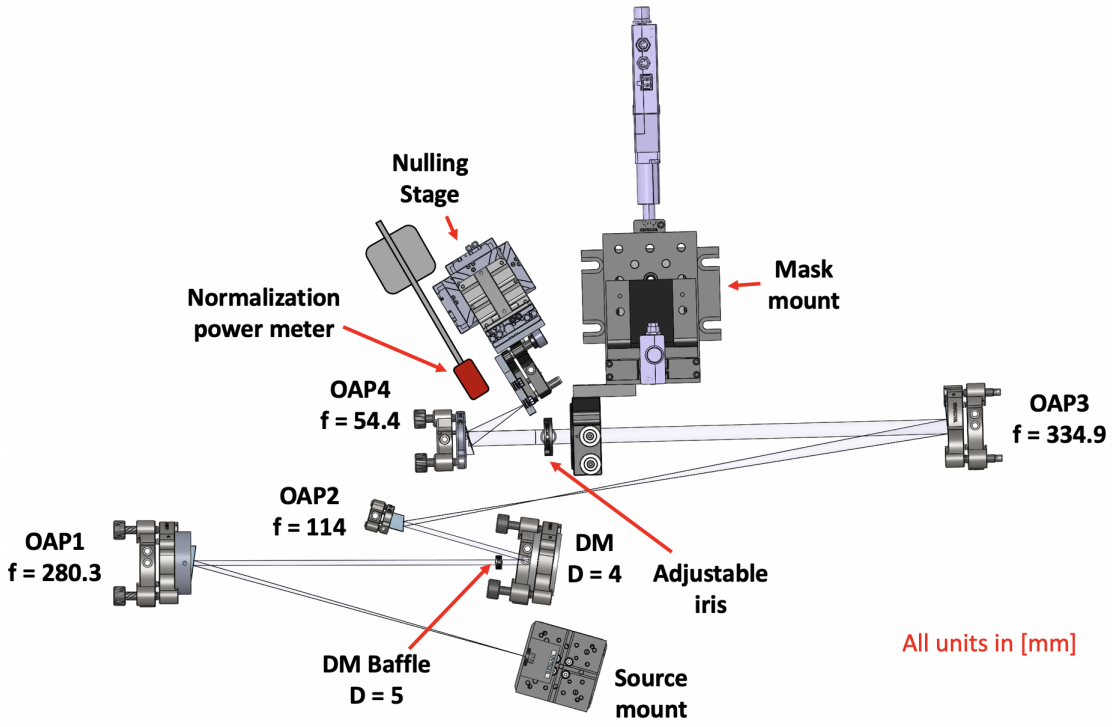

Figure 6. A light source is fed into the bench with a single-mode fiber mounted to the source stage. The light is collimated by an off-axis parabola (OAP) mirror. The collimated light is filtered by a baffle before reflecting off of a 12×12 Boston Micromachines deformable mirror (DM). Then, a set of relay OAPs magnifies the beam. In the resulting collimated beam is a mask mount that can be used to insert a pupil plane mask (such as a vortex); however, we leave it empty for this work. The beam then passes through an adjustable-size iris, which we use to control the $F\#$ of the system. The beam is then focused by the last OAP onto the injection stage, which holds both a single-mode fiber and the 6-port MSPL. The injection stage has translation controllers in all three axes, which allows light to be injected into either the SMF or the MSPL, and can also be used to scan the face of either optic across the focused beam. To measure the coupled flux through the SMF, the output end of the SMF is routed to a Femto OE-200 photodiode. To measure the coupled flux through one of the lantern ports, the SMF pigtail corresponding to that port is routed to the Femto photodiode. This setup can only measure one port at a time, so the measurements for the different ports are made sequentially. A Thorlabs S122C power meter on a retractable stage can be inserted into the beam just before the injection mount to measure its flux, which, after calibrating its readings to that of the Femto photodiode, can be used to normalize the coupled flux measurements to obtain throughput measurements.

the conversion between microns of translation on the injection stage and λ/D. Identifying this factor is part of planned future work.

To better resolve the central null, we repeat the scans, but with smaller spatial sampling by a factor of 5. The results are shown in Fig. 7c. Because the maps are asymmetric and the apparent centers of the modes slightly offset from each other, it is ambiguous which XY coordinate, even in simulation, should be designated as the theoretical axial center to which the star would be aligned. One approach, which we use for this work, is to sum up the central throughput maps of the four nulled ports (shown in Fig. 7d), and then take the location of minimum summed throughput as the center. The stellar leakages (η_s) at the identified center for each port are reported in Table 2.

In Table 1, we also report the values of $\eta_s/\eta_{p_{\text{peak}}}$. This value is often referred to as the 'null-depth' in discrete-aperture nulling interferometry contexts and as the 'raw contrast' in fiber-fed spectroscopy contexts. To avoid confusion, we will refer to it in this work explicitly as the quantity $\eta_s/\eta_{p_{\text{peak}}}$.

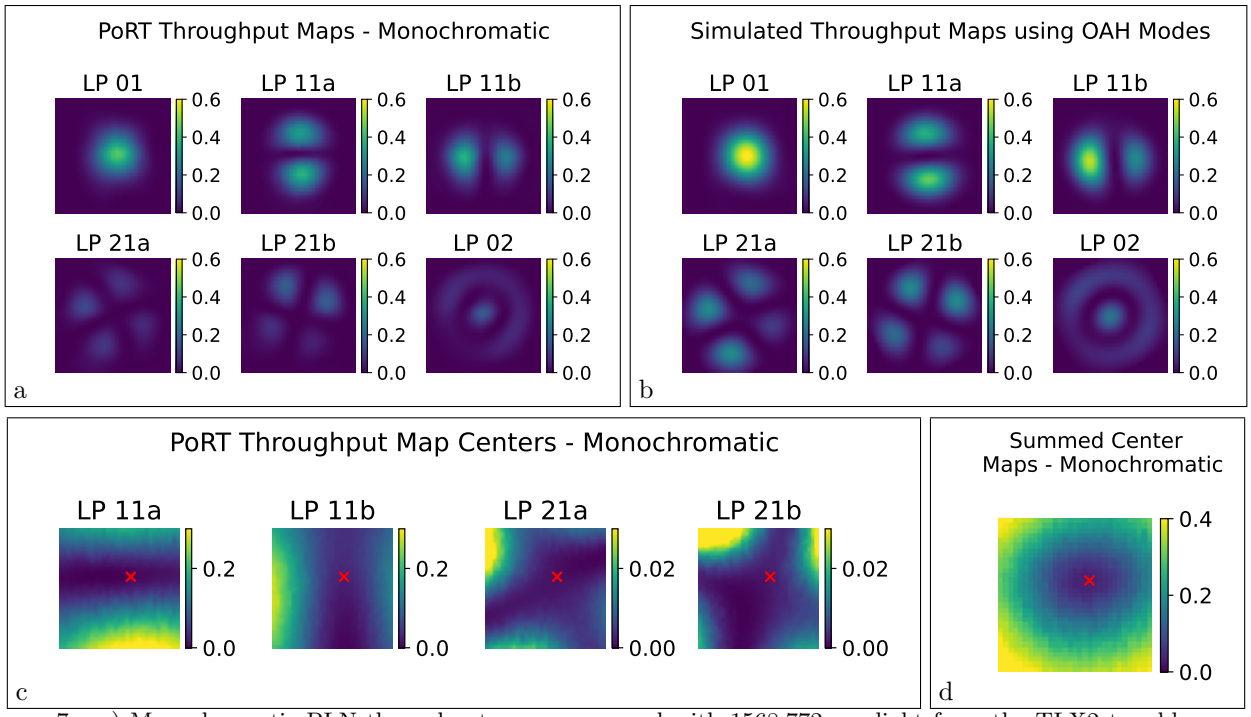

Figure 7. a) Monochromatic PLN throughput maps measured with 1568.772 nm light from the TLX2 tunable narrow linewidth laser on the PoRT testbed. b) Simulated throughput maps based on the mode profiles reconstructed using OAH at the same wavelength, assuming that the lantern is flux-preserving. c) Monochromatic PoRT throughput maps of the nulled ports with fine spatial sampling of the center. The red crosses indicate the axial center of the lantern, identified using the map in part (d). d) The summed throughput of the four maps in part (c). The location of minimum summed throughput is taken to be the lantern center, where η_s is measured.

3.2.2 Broadband

We repeat the same experiment using a broadband Super-Luminescent Diode (SLD) light source with wavelength coverage from 1450 nm to 1625 nm. The throughput maps are shown in Fig. 8. The peak and coaxial throughput values, as well as the ratio, determined using the same methodology as with monochromatic light, are reported in Table 2. The broadband nulls are not significantly different from the monochromatic ones (slightly higher in the LP 11 ports, about a factor of 2 higher in LP 21a, and about 20% lower in LP 21b), indicating that the lantern's response should be fairly achromatic. Future work includes measuring the actual spectral response of the lantern.

4. DISCUSSION AND FUTURE WORK

In Table 2, we also include the values for $\eta_{p_{\text{peak}}}$, η_s, and $\eta_s/\eta_{p_{\text{peak}}}$ obtained from the simulation using OAH modes. The simulated value of $\eta_s/\eta_{p_{\text{peak}}}$ assumes no wavefront error, so is indicative of the limit imposed by the modal impurities of the lantern. For three of the nulled ports, $\eta_s/\eta_{p_{\text{peak}}}$ is higher on the testbed than in simulation, but for the LP 21a port, it is lower. The difference suggests that the wavefront of the PoRT testbed, optimized for injection through a single-mode fiber, is still not perfectly flat. However, as indicated by the LP 21a port, where the testbed measured a lower value of $\eta_s/\eta_{p_{\text{peak}}}$ than in simulation (in both monochromatic and broadband light), a perfectly flat wavefront is not necessarily the optimal wavefront for a real PLN with modal impurities. Additional wavefront control methods could be used to optimize the wavefront and compensate, as much as possible, for the modal impurities of the lantern. This project is left for future work. However, even with $\eta_s/\eta_{p_{\text{peak}}}$ values of 10^{-2} to 10^{-3}, the PLN could be used to target spectroscopic observations of close-in giant exoplanets using ground based telescopes.

Table 2. Key PLN metrics from a) simulations using the modes measured with OAH assuming that the lantern is flux-preserving, b) measured on the PoRT testbed with a monochromatic laser, and c) measured on the PoRT testbed with a broadband SLD light source. $\eta_{p_{\text{peak}}}$ refers to the maximum throughput of each map, or what the throughput of a planet at the location of maximum coupling would be. For the nulled ports, η_s refers to the throughput at the coaxial center of the lantern, corresponding to the stellar leakage. For the nulled ports, we also report the ratio $\eta_s/\eta_{p_{\text{peak}}}$, often called the 'null-depth' in discrete-aperture interferometry contexts or 'raw contrast' in fiber-fed spectroscopy contexts.

	LP 01	**LP 11a**	**LP 11b**	**LP 21a**	**LP 21b**	**LP 02**
$\eta_{p_{\text{peak}}}$ (Simulation)	0.614	0.461	0.542	0.287	0.285	0.233
$\eta_{p_{\text{peak}}}$ (PoRT, Monochromatic)	0.446	0.387	0.380	0.135	0.179	0.171
$\eta_{p_{\text{peak}}}$ (PoRT, Broadband)	0.441	0.383	0.393	0.138	0.191	0.192
η_s (Simulation)	N/A	7.42×10^{-4}	3.03×10^{-3}	6.44×10^{-3}	9.44×10^{-4}	N/A
η_s (PoRT, Monochromatic)	N/A	4.91×10^{-3}	2.90×10^{-2}	1.23×10^{-3}	2.24×10^{-3}	N/A
η_s (PoRT, Broadband)	N/A	7.60×10^{-3}	3.11×10^{-2}	2.65×10^{-3}	2.02×10^{-3}	N/A
$\eta_s/\eta_{p_{\text{peak}}}$ (Simulation)	N/A	1.61×10^{-3}	5.55×10^{-3}	2.24×10^{-2}	3.29×10^{-3}	N/A
$\eta_s/\eta_{p_{\text{peak}}}$ (PoRT, Monochromatic)	N/A	1.27×10^{-2}	7.62×10^{-2}	9.11×10^{-3}	1.25×10^{-2}	N/A
$\eta_s/\eta_{p_{\text{peak}}}$ (PoRT, Broadband)	N/A	1.96×10^{-2}	7.92×10^{-2}	1.93×10^{-2}	1.06×10^{-2}	N/A

More immediate plans include identifying the conversion between microns of translation on the injection stage and units of λ/D, as well as the subsequent careful alignment of the simulation coordinates to testbed coordinates.

In our monochromatic experiment, we only probed one polarization, with a polarization maintaining (PM) fiber connected to the source. We plan to test the orthogonal polarization by adding a 90 degree polarization rotating fiber. Our broadband measurements were taken using a standard (non-PM) fiber connected to the source, so the polarization is unknown. We plan to repeat the broadband measurements using two orthogonal polarization states as well.

We also plan to take spectrally-resolved measurements of η_s and $\eta_{p_{\text{peak}}}$ through the lantern. By comparing the spectrally-resolved measurements for each port, we will be able to characterize the spectral response of the PLN.

ACKNOWLEDGMENTS

Y.X acknowledges support from the National Science Foundation Graduate Research Fellowship under Grant No. 1122374. Additional effort has been supported by the National Science Foundation under Grant No. 2109231. This research was carried out in part at the California Institute of Technology and the Jet Propulsion Laboratory under a contract with the National Aeronautics and Space Administration (NASA).

This research made use of hcipy;[11] Astropy;[12–14] NumPy;[15] SciPy;[16] and Matplotlib.[17]

REFERENCES

[1] National Research Council, [*Pathways to Discovery in Astronomy and Astrophysics for the 2020s*], The National Academies Press, Washington, DC (2021).

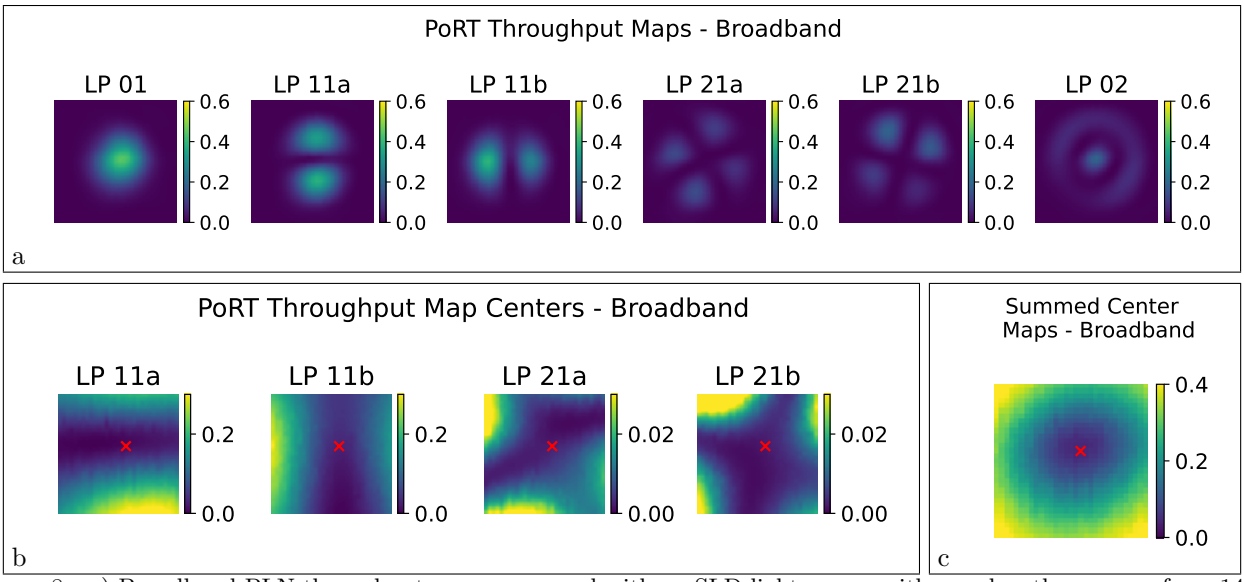

Figure 8. a) Broadband PLN throughput maps measured with an SLD light source with wavelength coverage from 1450 nm to 1625 nm on the PoRT testbed. b) Broadband PoRT throughput maps of the nulled ports with fine spatial sampling of the center. The red crosses indicate the axial center of the lantern, identified using the map in part (c). c) The summed throughput of the four maps in part (b). The location of minimum summed throughput is taken to be the lantern center, where η_s is measured.

[2] Wang, J., Mawet, D., Ruane, G., Hu, R., and Benneke, B., "Observing Exoplanets with High Dispersion Coronagraphy. I. The Scientific Potential of Current and Next-generation Large Ground and Space Telescopes," *The Astronomical Journal* **153**, 183 (Apr. 2017).

[3] Ruffio, J.-B., Horstman, K., Mawet, D., Rosenthal, L. J., Batygin, K., Wang, J. J., Millar-Blanchaer, M., Wang, J., Fulton, B. J., Konopacky, Q. M., Agrawal, S., Hirsch, L. A., Howard, A. W., Blunt, S., Nielsen, E., Baker, A., Bartos, R., Bond, C. Z., Calvin, B., Cetre, S., Delorme, J.-R., Doppmann, G., Echeverri, D., Finnerty, L., Fitzgerald, M. P., Jovanovic, N., López, R., Martin, E. C., Morris, E., Pezzato, J., Ruane, G., Sappey, B., Schofield, T., Skemer, A., Venenciano, T., Wallace, J. K., Wallack, N. L., Wizinowich, P., and Xuan, J. W., "Detecting Exomoons from Radial Velocity Measurements of Self-luminous Planets: Application to Observations of HR 7672 B and Future Prospects," *The Astronomical Journal* **165**, 113 (Mar. 2023).

[4] Xin, Y., Jovanovic, N., Ruane, G., Mawet, D., Fitzgerald, M. P., Echeverri, D., Lin, J., Leon-Saval, S., Gatkine, P., Kim, Y. J., Norris, B., and Sallum, S., "Efficient Detection and Characterization of Exoplanets within the Diffraction Limit: Nulling with a Mode-selective Photonic Lantern," **938**, 140 (Oct. 2022).

[5] Tuthill, P., "Nulling interferometry: high contrast science for single large apertures," in [*Adaptive Optics Systems VIII*], Schreiber, L., Schmidt, D., and Vernet, E., eds., **12185**, 121858P, International Society for Optics and Photonics, SPIE (2022).

[6] Ruane, G., Wang, J., Mawet, D., et al., "Efficient spectroscopy of exoplanets at small angular separations with vortex fiber nulling," *Astrophys. J.* (2018).

[7] Echeverri, D., Ruane, G., Jovanovic, N., Mawet, D., and Levraud, N., "Vortex fiber nulling for exoplanet observations I Experimental demonstration in monochromatic light," *Optics Letters* **44**, 2204 (May 2019).

[8] Leon-Saval, S. G., Fontaine, N. K., Salazar-Gil, J. R., Ercan, B., Ryf, R., and Bland-Hawthorn, J., "Mode-selective photonic lanterns for space-division multiplexing," *Opt. Express* **22**, 1036–1044 (Jan 2014).

[9] Leon-Saval, S. G., Argyros, A., and Bland-Hawthorn, J., "Photonic lanterns," *Nanophotonics* **2**, 429–440 (Dec. 2013).

[10] Cuche, E., Marquet, P., and Depeursinge, C., "Spatial filtering for zero-order and twin-image elimination in digital off-axis holography," *Appl. Opt.* **39**, 4070–4075 (Aug 2000).

[11] Por, E. H., Haffert, S. Y., Radhakrishnan, V. M., Doelman, D. S., Van Kooten, M., and Bos, S. P., "High Contrast Imaging for Python (HCIPy): an open-source adaptive optics and coronagraph simulator," in [*Adaptive Optics Systems VI*], *Proc. SPIE* **10703** (2018).

[12] Astropy Collaboration, Robitaille, T. P., Tollerud, E. J., Greenfield, P., Droettboom, M., Bray, E., Aldcroft, T., Davis, M., Ginsburg, A., Price-Whelan, A. M., Kerzendorf, W. E., Conley, A., Crighton, N., Barbary, K., Muna, D., Ferguson, H., Grollier, F., Parikh, M. M., Nair, P. H., Unther, H. M., Deil, C., Woillez, J., Conseil, S., Kramer, R., Turner, J. E. H., Singer, L., Fox, R., Weaver, B. A., Zabalza, V., Edwards, Z. I., Azalee Bostroem, K., Burke, D. J., Casey, A. R., Crawford, S. M., Dencheva, N., Ely, J., Jenness, T., Labrie, K., Lim, P. L., Pierfederici, F., Pontzen, A., Ptak, A., Refsdal, B., Servillat, M., and Streicher, O., "Astropy: A community Python package for astronomy," *Astronomy and Astrophysics* **558**, A33 (Oct. 2013).

[13] Price-Whelan, A. M., Sipőcz, B. M., Günther, H. M., Lim, P. L., Crawford, S. M., Conseil, S., Shupe, D. L., Craig, M. W., Dencheva, N., Ginsburg, A., VanderPlas, J. T., Bradley, L. D., Pérez-Suárez, D., de Val-Borro, M., Paper Contributors, P., Aldcroft, T. L., Cruz, K. L., Robitaille, T. P., Tollerud, E. J., Coordination Committee, A., Ardelean, C., Babej, T., Bach, Y. P., Bachetti, M., Bakanov, A. V., Bamford, S. P., Barentsen, G., Barmby, P., Baumbach, A., Berry, K. L., Biscani, F., Boquien, M., Bostroem, K. A., Bouma, L. G., Brammer, G. B., Bray, E. M., Breytenbach, H., Buddelmeijer, H., Burke, D. J., Calderone, G., Cano Rodríguez, J. L., Cara, M., Cardoso, J. V. M., Cheedella, S., Copin, Y., Corrales, L., Crichton, D., D'Avella, D., Deil, C., Depagne, É., Dietrich, J. P., Donath, A., Droettboom, M., Earl, N., Erben, T., Fabbro, S., Ferreira, L. A., Finethy, T., Fox, R. T., Garrison, L. H., Gibbons, S. L. J., Goldstein, D. A., Gommers, R., Greco, J. P., Greenfield, P., Groener, A. M., Grollier, F., Hagen, A., Hirst, P., Homeier, D., Horton, A. J., Hosseinzadeh, G., Hu, L., Hunkeler, J. S., Ivezić, Ž., Jain, A., Jenness, T., Kanarek, G., Kendrew, S., Kern, N. S., Kerzendorf, W. E., Khvalko, A., King, J., Kirkby, D., Kulkarni, A. M., Kumar, A., Lee, A., Lenz, D., Littlefair, S. P., Ma, Z., Macleod, D. M., Mastropietro, M., McCully, C., Montagnac, S., Morris, B. M., Mueller, M., Mumford, S. J., Muna, D., Murphy, N. A., Nelson, S., Nguyen, G. H., Ninan, J. P., Nöthe, M., Ogaz, S., Oh, S., Parejko, J. K., Parley, N., Pascual, S., Patil, R., Patil, A. A., Plunkett, A. L., Prochaska, J. X., Rastogi, T., Reddy Janga, V., Sabater, J., Sakurikar, P., Seifert, M., Sherbert, L. E., Sherwood-Taylor, H., Shih, A. Y., Sick, J., Silbiger, M. T., Singanamalla, S., Singer, L. P., Sladen, P. H., Sooley, K. A., Sornarajah, S., Streicher, O., Teuben, P., Thomas, S. W., Tremblay, G. R., Turner, J. E. H., Terrón, V., van Kerkwijk, M. H., de la Vega, A., Watkins, L. L., Weaver, B. A., Whitmore, J. B., Woillez, J., Zabalza, V., and Contributors, A., "The Astropy Project: Building an Open-science Project and Status of the v2.0 Core Package," *Astronomical Journal* **156**, 123 (Sept. 2018).

[14] Astropy Collaboration, Price-Whelan, A. M., Lim, P. L., Earl, N., Starkman, N., Bradley, L., Shupe, D. L., Patil, A. A., Corrales, L., Brasseur, C. E., Nöthe, M., Donath, A., Tollerud, E., Morris, B. M., Ginsburg, A., Vaher, E., Weaver, B. A., Tocknell, J., Jamieson, W., van Kerkwijk, M. H., Robitaille, T. P., Merry, B., Bachetti, M., Günther, H. M., Aldcroft, T. L., Alvarado-Montes, J. A., Archibald, A. M., Bódi, A., Bapat, S., Barentsen, G., Bazán, J., Biswas, M., Boquien, M., Burke, D. J., Cara, D., Cara, M., Conroy, K. E., Conseil, S., Craig, M. W., Cross, R. M., Cruz, K. L., D'Eugenio, F., Dencheva, N., Devillepoix, H. A. R., Dietrich, J. P., Eigenbrot, A. D., Erben, T., Ferreira, L., Foreman-Mackey, D., Fox, R., Freij, N., Garg, S., Geda, R., Glattly, L., Gondhalekar, Y., Gordon, K. D., Grant, D., Greenfield, P., Groener, A. M., Guest, S., Gurovich, S., Handberg, R., Hart, A., Hatfield-Dodds, Z., Homeier, D., Hosseinzadeh, G., Jenness, T., Jones, C. K., Joseph, P., Kalmbach, J. B., Karamehmetoglu, E., Kałuszyński, M., Kelley, M. S. P., Kern, N., Kerzendorf, W. E., Koch, E. W., Kulumani, S., Lee, A., Ly, C., Ma, Z., MacBride, C., Maljaars, J. M., Muna, D., Murphy, N. A., Norman, H., O'Steen, R., Oman, K. A., Pacifici, C., Pascual, S., Pascual-Granado, J., Patil, R. R., Perren, G. I., Pickering, T. E., Rastogi, T., Roulston, B. R., Ryan, D. F., Rykoff, E. S., Sabater, J., Sakurikar, P., Salgado, J., Sanghi, A., Saunders, N., Savchenko, V., Schwardt, L., Seifert-Eckert, M., Shih, A. Y., Jain, A. S., Shukla, G., Sick, J., Simpson, C., Singanamalla, S., Singer, L. P., Singhal, J., Sinha, M., Sipőcz, B. M., Spitler, L. R., Stansby, D., Streicher, O., Šumak, J., Swinbank, J. D., Taranu, D. S., Tewary, N., Tremblay, G. R., de Val-Borro, M., Van Kooten, S. J., Vasović, Z., Verma, S., de Miranda Cardoso, J. V., Williams, P. K. G., Wilson, T. J., Winkel, B., Wood-Vasey, W. M., Xue, R., Yoachim, P., Zhang, C., Zonca, A., and Astropy Project Contributors, "The Astropy Project: Sustaining

and Growing a Community-oriented Open-source Project and the Latest Major Release (v5.0) of the Core Package," **935**, 167 (Aug. 2022).

[15] Harris, C. R., Millman, K. J., van der Walt, S. J., Gommers, R., Virtanen, P., Cournapeau, D., Wieser, E., Taylor, J., Berg, S., Smith, N. J., Kern, R., Picus, M., Hoyer, S., van Kerkwijk, M. H., Brett, M., Haldane, A., del Río, J. F., Wiebe, M., Peterson, P., Gérard-Marchant, P., Sheppard, K., Reddy, T., Weckesser, W., Abbasi, H., Gohlke, C., and Oliphant, T. E., "Array programming with NumPy," *Nature* **585**, 357–362 (Sept. 2020).

[16] Virtanen, P., Gommers, R., Oliphant, T. E., Haberland, M., Reddy, T., Cournapeau, D., Burovski, E., Peterson, P., Weckesser, W., Bright, J., van der Walt, S. J., Brett, M., Wilson, J., Jarrod Millman, K., Mayorov, N., Nelson, A. R. J., Jones, E., Kern, R., Larson, E., Carey, C., Polat, İ., Feng, Y., Moore, E. W., Vand erPlas, J., Laxalde, D., Perktold, J., Cimrman, R., Henriksen, I., Quintero, E. A., Harris, C. R., Archibald, A. M., Ribeiro, A. H., Pedregosa, F., van Mulbregt, P., and Contributors, S. . ., "SciPy 1.0: Fundamental Algorithms for Scientific Computing in Python," *Nature Methods* **17**, 261–272 (2020).

[17] Hunter, J. D., "Matplotlib: A 2D graphics environment," *Computing in Science & Engineering* **9**(3), 90–95 (2007).